*Revised Manuscript with No Changes Marked
Click here to download Revised Manuscript with No Changes Marked: Final_Manuscript_8-20-18_Clean.docx

Identifying Degradation Mechanisms in Lithium-Ion Batteries with Coating Defects at the Cathode

Lamuel David,[a] Rose E. Ruther,[a] Debasish Mohanty,[a] Harry M. Meyer III,[b] Yangping Sheng,[a] Sergiy Kalnaus,[c] Claus Daniel,[a,d] and David L. Wood III[a,d,*]

[a]Energy and Transportation Science Division, Oak Ridge National Laboratory, Oak Ridge, TN, 37831-6083, USA

[b]Material Science and Technology Division, Oak Ridge National Laboratory, Oak Ridge, TN, 37831-6083, USA

[c]Computational Sciences and Engineering Division, Oak Ridge National Laboratory, Oak Ridge, TN, 37831-6083, USA

[d]Bredesen Center for Interdisciplinary Research and Graduate Education, University of Tennessee, Knoxville, Tennessee 37996, USA

Correspondence and requests for materials should be addressed to David L. Wood III, 2370 Cherahala Boulevard, Knoxville, TN 37932-6479 (wooddl@ornl.gov)

This manuscript has been authored by UT-Battelle, LLC under Contract No. DE-AC05-00OR22725 with the U.S. Department of Energy. The United States Government retains and the publisher, by accepting the article for publication, acknowledges that the United States Government retains a non-exclusive, paid-up, irrevocable, world-wide license to publish or reproduce the published form of this manuscript, or allow others to do so, for United States Government purposes. The Department of Energy will provide public access to these results of federally sponsored research in accordance with the DOE Public Access Plan (http://energy.gov/downloads/doe-public-access-plan).

Abstract

Understanding the effect of electrode manufacturing defects on lithium-ion battery (LIB) performance is key to reducing the scrap rate and cost during cell manufacturing. In this regard, it is necessary to quantify the impact of various defects that are generated during the electrode coating process. To this end, we have tested large-format 0.5Ah $LiNi_{0.5}Mn_{0.3}Co_{0.2}O_2$/graphite pouch cells with defects intentionally introduced into the cathode coating. Different types of coating defects were tested including agglomerates, pinholes, and non-uniform coating. Electrodes with larger non-coated surface had greater capacity fade than baseline electrodes, while pinholes and agglomerates did not affect performance adversely. Post cycle analysis of electrodes showed that the anode facing the defective region in the cathode was clearly impacted by the defect. Further characterization using Raman spectroscopy, X-ray photoelectron spectroscopy, and X-ray diffraction provided evidence for a proposed mechanism for material degradation related to the most detrimental type of coating defect.

Keywords: Li-ion battery, manufacturing, electrode coating, Raman mapping, XPS, computational modeling

1. Introduction

Lithium-ion batteries (LIBs) have been successfully commercialized in portable electronic devices.[1, 2] However, batteries for electric vehicles (EVs), hybrid electric vehicles (HEVs), and plug-in hybrid electric vehicles (PHEVs)[3] have stricter requirements like lighter weight, longer range, improved safety, and longer cycle life.[4] EV batteries need to be cost-effective as well. The latest EV cell cost target from the US Department of Energy (DOE) is $80/kWh with a useable energy density of 750

Wh/L and a peak power density of 1500 W/L by 2020. This is a very aggressive target, since the current cells for electric vehicles cost around $245/kWh and have an energy density around 285 Wh/L.[5] The cost of expensive metals like cobalt, nickel, and lithium is a major component of the final price of LIBs.[6] On this subject, there is growing research aimed towards lowering the cost of materials in LIBs.[7] However, any change in the battery materials has to undergo a rigorous testing phase to address strict safety requirements and to exhibit equivalent or improved battery performance.[8] Therefore, new material technologies require long periods for implementation. To tackle the immediate need for cost reduction, there is a growing demand to reduce the manufacturing costs to offset high material costs.[9]

There are several methods to reduce electrode manufacturing cost through advanced material processing and material handling technologies. These include adapting cheaper water-based solvents, developing solvent-free coating,[10] or implementing spray/electrostatic coating methods.[11] However, changing processing technologies at an existing battery manufacturing plant requires a high capital cost. Another method to reduce cost without large capital investment is to improve quality control practices to reduce scrap rates. The cost of raw materials in the electrode is high, and coating defects are one of the primary sources of waste in battery manufacturing. The current quality control process involves discarding defective coatings regardless of the type of defect and using only ideal electrode coatings, potentially contributing to excessive waste. The quality of the electrode coating depends on uniform thickness, porosity,[12] material distribution (areal weight), and adhesion to the current collector.[13] Any inhomogeneity of these properties results in defects[14] that lead to local aging of the electrode with loss in capacity and cycle life.[15]

In this study, we evaluate the effect of electrode inhomogeneities on the electrochemical behavior of lithium-ion batteries. We analyzed the electrochemical properties of three types of coating defects in cathodes: (a) pinholes, (b) agglomerates, and (c) line defects. In our previous study, we used coin cells for analysis which showed that defects in electrode coating significantly impacted electrochemical performance.[16] However, the study was influenced by cell-to-cell variations, and the fraction of defective area relative to the total electrode area was large, which exaggerated the influence of the defect. To overcome these limitations, we continued our studies using large-format multilayer pouch cells, which closely resembled industrial battery manufacturing conditions. To our knowledge this is the first study to evaluate the impact of different types of coating defects on the electrochemical performance of lithium-ion batteries under conditions that replicate state-of-the-art electrode coating and

cell manufacturing. Cell testing was performed using a rigorous protocol to accelerate the degradation process. Further, chemical characterization using Raman spectroscopy, X-ray photoelectron spectroscopy (XPS), and X-ray diffraction (XRD) was performed on the harvested electrodes to determine the mechanism of degradation and the extent to which it influences electrochemical properties. As in our previous study,[16] the electrode defects were specifically generated in a controlled manner to standardize the experiment. By better understanding how cells with coating defects behave, we are able to determine if these coatings are suitable for other applications. For example, electrodes with some defects could possibly be used in low-power or low-energy applications like grid-storage or backup power storage devices instead of becoming waste.

2. Experimentation and methods

2.1.Materials and electrode fabrication

The electrodes were fabricated at the U.S. Department of Energy (DOE) Battery Manufacturing R&D Facility at Oak Ridge National Laboratory. Anode and cathode slurries were prepared by dispersing the active material, binder, and conductive additives in *N*-Methyl-2-pyrrolidone with a planetary mixer (Ross PDM-1/2). The cathode consisted of $LiNi_{0.5}Mn_{0.3}Co_{0.2}O_2$ powder (NMC532, Toda America Inc., 90 wt.%), polyvinylidene fluoride (PVDF, Solvay 5130, 5 wt.%), and carbon black (Denka, 5 wt.%). The anode contained natural graphite (ConocoPhillips, A12, 92 wt.%), PVDF (Kureha 9300, 6 wt.%), and Super P Li (Timcal, 2 wt.%). The slurries were applied with a slot-die coater (Frontier Industrial Technology, Inc.) to one side of a foil current collector (15 μm thick Al for the cathode and 9 μm thick Cu for the anode). The active material loadings for the cathode and anode were 15.0 mg/cm^2 (2.4 mAh/cm^2) and 8.0 mg/cm^2 (2.88 mAh/cm^2), respectively, yielding a negative to positive capacity ratio (n/p ratio) of 1.2. Electrodes were calendared to 35% porosity.

2.2.Pouch cell assembly

Full pouch cells with 500 mAh capacity were built using the electrodes that were dried in a vacuum oven for 24 hr. The pouch cells consisted of six anodes and six cathodes stacked alternately with a porous polymer separator (Celgard 2325). The electrolyte was a 1.2 M solution of $LiPF_6$ in ethylene carbonate (EC) and ethyl methyl carbonate (EMC) (3:7 ratio by weight) (SoulBrain, MI). The electrolyte fill factor, defined as the ratio of the electrolyte volume to the total pore volume in the cell, was 1.6.

2.3.Electrochemical Testing

Electrochemical testing was carried out using a Maccor battery cycler. Cells were cycled within a voltage window of 3.0-4.2 V. Cells first underwent 4 formation cycles at C/10 charge and discharge rate followed by 500 aging cycles at 1C rate (1C = 160 mA/g_{NMC}). The cell voltage was held at 4.2 V for 3 hours at the end of each charge during the aging cycling. Every 50 cycles the cells underwent a deep discharge with a constant voltage hold until the current dropped to C/20. A DC resistance test, hybrid pulse power characterization (HPPC), was performed after formation cycling and after every 50 cycles during discharge. The HPPC protocol included one full cycle at C/10 rate followed by one full cycle at C/3 rate to prepare the cell for characterization. The cell was recharged to 4.2 V at C/3 rate and the HPPC was performed during discharge at C/3 rate at every 10% state of charge (SOC). The HPPC protocol starts with a one-hour rest step followed by a discharge pulse at 2C for 10 seconds and a regeneration pulse at 1.5C for 10 seconds. There is a rest step for 40 seconds before and after the regeneration pulse. Three cells were cycled for each type of defect to standardize the results. After cycling, the cells were disassembled in an argon-filled glove box, and the cycled electrodes were soaked in DMC solvent for 1 min to remove residual electrolyte prior to post-mortem characterization.

2.4.Microstructural Characterization

2.4.1. FTIR. Fourier-transform infrared spectra were collected in attenuated total reflectance (ATR) mode with a germanium crystal. The FTIR instrument (Bruker Alpha) was housed in an argon-filled glove box to prevent air exposure.

2.4.2. Raman Spectroscopy. For Raman spectroscopy, anodes were sealed under glass inside an argon-filled glove box to prevent exposure to air. Raman spectra were acquired with an Alpha 300 confocal Raman microscope (WITec, GmbH) using a solid-state 532 nm excitation laser, a 20X objective, and 600 grooves/mm grating. The laser spot size was approximately 1 μm. Raman maps were acquired over 100 μm x 100 μm areas of the anodes in 1 μm x 1 μm steps with an integration time of 15 sec/pixel. The laser power was attenuated to 1 mW to prevent damage to the sample from laser-induced heating. Raman maps were analyzed using Witec ProjectPlus software.

2.4.3. XPS. X-ray photoelectron spectroscopy (XPS) was performed using a Thermo Scientific (Waltham, MA, USA) Model K-Alpha XPS instrument. The instrument utilizes a monochromated,

micro-focusing, Al Kα X-ray source (1486.6 eV). Analyses of the samples were all conducted with a 400 μm X-ray spot size for maximum signal and to obtain an average surface composition over the largest possible area. The instrument has a hemispherical electron energy analyzer equipped with a 128 multi-channel detector system. The base pressure in the analysis chamber is typically 2 x 10^{-9} mbar or lower. The samples were transferred from an argon filled glove box in a special vacuum transfer system to the XPS instrument to prevent air exposure. Specific areas were chosen for analysis by viewing the samples with a digital optical camera with a magnification of approximately 60-200X. For depth profiles, an Ar-ion gun operated at 2 kV and 10 nA was used. The samples were sputtered for 120 s. All spectra were acquired with the charge neutralization flood gun turned on to maintain stable analysis conditions. The flood gun uses a combination of low energy electrons and argon ions for optimum charge compensation. The typical pressure in the analysis chamber with the flood gun operating is 2 x 10^{-7} mbar. Data were collected using the Thermo Scientific Avantage XPS software package (v.4.61).

2.4.4. XRD. X-ray diffraction was performed using a PANalytical X'Pert system with a Cu source (λ = 1.54 Å) and automatic divergence and anti-scatter slits operated at 45 kV and 40 mA. The electrode samples were placed in a holder with a thin Kapton film to reduce exposure to moisture. The sample was rotated during data collection to average the region from which the diffracted X-ray signals were collected. The electrode sample size was approximately 1 cm x 1 cm. Signal was collected between 10-80° 2θ at a scan rate of 20 min/scan.

2.5. Computational Modeling

A formulation based on porous electrode theory with mass balance in both solid and liquid phases was applied including Butler-Volmer process for the charge transfer. The system of equations describing electrochemical reactions and mass transport has been reported elsewhere[17] and will not be repeated here for the purpose of brevity. Finite elements (FE) solution was performed using COMSOL Multiphysics software on a 16-core workstation. Charge of the as assembled electrode pair was modeled with variable time stepping and an applied current density of 8 A/m^2, which corresponds to 1C charge.

3. Results and Discussion

Defects generated during coating can be broadly classified into four categories as outlined in our previous paper.[16] They are (1) agglomerates (blisters), (2) pinholes (divots), (3) line defects and (4)

metal particle contamination. Of these defects, metal particle contamination is the most detrimental, but it can be managed by maintaining a clean and dust-free coating environment. The schematic in Fig. 1 shows the three kinds of defects that are primarily generated during slurry processing and are much harder to manage as the slurry can vary from batch to batch. The source of each of these defects is briefly explained in this section. (1) Agglomeration of material can be caused by improper mixing, which produces large separated regions of electrode components. This leads to poorer conduction and transport within the agglomerates, which results in localized impedance rise and capacity loss. In this experiment, agglomerates were formed by adding a small amount of active material and conductive additive in the appropriate ratios to the slurry at the end of the mixing process. Agglomerates formed by this method were approximately 50-100 μm across (measured by visual inspection), and there were 15-20 agglomerates per electrode (total electrode area: 56 x 84.4 mm). (2) Pinholes can be formed by air bubbles that are present in the slurry during coating. This leads to localized regions where the n/p ratio is off target and possible exposure of the current collector to the electrolyte. In this study, pinholes were formed by removing a small amount of material from a baseline electrode using a pointed object. Care was taken to protect the underlying current collector. As seen in Fig. 1, pinholes formed by this method were approximately 100-200 μm across (measured by visual inspection) with 6-8 pinholes for each electrode. (3) Line defects are formed when there is an obstruction in the slot-die coater. This forms a region of the uncoated area in the form of a line on the electrode. The size of the exposed region depends on the size of the obstruction. These uncoated regions distort the n/p ratio and expose the current collector. As in our previous study,[16] we designed a special coating attachment which forms these defects in two types. (a) 3X-Line defect: Three uncoated lines that are 1 mm in width and spaced 3 mm apart (b) 1X-Line defect: One uncoated line 3 mm in width.

3.1.Electrochemical Characterization

Large-format 0.5 Ah pouch cells (volume of 6x9x0.4 cm^3) with various defects and baseline cells (with no defects) were subjected to cycle life testing for 500 cycles at 1C/-1C rate between 3-4.2 V (Fig. 2a). The breaks in cycling every 50 cycles were from the hybrid pulse power characterization (HPPC) step that was included in the cycling protocol. All the cells had a first cycle charge capacity of 183-189 mAh/g_{NMC} during formation (Supplementary Fig. S1) followed by discharge capacities of 150-155 mAh/g_{NMC}, yielding a first cycle efficiency between 81-84%. Charge/discharge curves of the first two formation cycles show little appreciable difference between the different defects (Supplementary Fig. S2

a,b). This is further confirmed by analyzing the differentiated voltage profiles (Supplementary Fig. S3 a,b). The peak around ~3 V is typical for the formation of the solid electrolyte interphase (SEI). The SEI formation was followed by two distinct cathode delithiation peaks at ~3.55 V and ~3.67 V, which correspond to $Ni^{2+/3+}$ and $Ni^{3+/4+}$ respectively, during the charge cycle.[18] All the cells had two distinct discharge peaks at ~3.61 V and ~3.45 V, respectively.

When the cells were further cycled during ageing at 1C/-1C rate, all the cells had a first cycle capacity of 147-151 mAh/g (the same within statistical error limits) (Fig. 2b and Supplementary Fig. S2c). The dQ/dV plot of the 1^{st} ageing cycle shows two distinct peaks at 3.58 V and 3.7 V during charge, which corresponds to $Ni^{2+/3+}$ and $Ni^{3+/4+}$ conversion respectively, for all the cells (Fig. 2d and Supplementary Fig. S3c). During discharge, one distinct peak corresponding to Li insertion was observed at 3.51 V.[18] On further cycling all cells lose capacity almost immediately due to the aggressive cycling protocol, which is designed to accelerate aging (Supplementary Fig. S4 and S5). The dQ/dV plots show that the degradation was most severe in the cells with line defects where the two distinct charge peaks from the first cycle at ~3.66 V and ~3.5 V converge to one large peak around ~3.7 V, and the discharge peak also shifts to ~3.45 V from ~3.5 V. Cells with 1X-line defects degrade at a faster rate almost immediately (Fig. 2 and Supplementary Fig. S2 d,e,f). The dQ/dV plot for the 25^{th} cycle in Supplementary Fig. S3d shows that for the 1X-line defect the charge peak at ~3.59 V has almost disappeared. There is also a general shift to higher voltage indicating higher impedance in the cell. Cells with pinholes and agglomerates and baseline cells retain two charge peaks, even though they are not as distinct as in the first cycle. The discharge capacities of baseline cells and cells with pinholes in the electrodes, overlap each other almost up to the end of the cycling protocol. However, pinholes exhibit lower energy efficiency at 88.88% when compared to baseline at 89.34 % (Supplementary Table S1). Cells with electrodes containing agglomerates initially had lower reversible capacity than the baseline cells, but they showed unusually stable long-term capacity retention. However, we also observed merging of the charging cycle peaks in the dQ/dV plot (Fig. 2e) in the 500^{th} cycle and a shift to higher voltage compared to baseline and pinhole cells which indicates material degradation and impedance rise. Additional studies with varying amounts of agglomeration are needed to fully understand their effect in electrochemical cycling behavior. In the case of the 1X-line defect, capacity fade occurs at a greater rate from the very first cycle until approximately the 50^{th} cycle when compared to the 3X-line defect. Beyond the 50^{th} cycle the capacity fade remained the same between 1X and 3X-line defects, but it was greater when compared to the baseline cell. Moreover, 1X-line defect had the lest efficiency at 86.47%,

which is considerably lower than baseline at 89.34%. (Supplementary Table S1). In general, the rate of degradation in all cells is greater compared to cells cycled with more standard protocols commonly found in the literature. The rapid fade is due to the 3-hour voltage hold at the end of the charge cycle, which was added in the protocol to accelerate electrode degradation and efficiently screen for the impact of defects.

3.2.Post Cycle Analysis

Representative anode and cathode pairs from cycled cells are shown in Fig. 3. All the cathodes appeared unchanged, while the anodes were mostly a mixture of gold, blue, and grey colors. The gold color is typical of fully lithiated graphite, LiC_6 and the blue color is attributed to partial Li intercalation into every other carbon-gallery, LiC_{12}. The grey color is attributed to surface film on the graphite surface.[19]

Anodes harvested from the cells with baseline, pinhole, and agglomerate cathodes showed similar color patterns in general. However, regions of the anodes that were cycled opposite pinhole defects showed distinct grey spots mirroring the defect in the cathode. With line defects the anodes were a mix of gold and blue color far from the defect due to lithium trapping. Directly opposite to the line defects the anodes remained grey in color, because this region did not participate in Li cycling (discussed later in the manuscript). Further characterization was performed to better understand the variations observed in the electrodes with line defects. Different regions in the 1X-Line defect were investigated: far away from the defect, near the defect and opposite or on the defect. Uncycled and cycled baseline anode were used as references.

3.2.1. Fourier Transform Infrared Spectroscopy (FTIR)

FTIR absorbance spectra were obtained in an Ar filled glove box. Supplementary Fig. S6a compares the absolute absorption values before baseline correction of the pristine uncycled anode to different regions on cycled anodes. The comparison shows that the uncycled anode spectrum generally had higher absorbance, while all the cycled anode spectra had lower IR absorbance. Interestingly, absorbance of the region opposite to the defect was intermediate between the uncycled anode and the other regions of the cycled anode. The increased absorbance in the region opposite to the defect suggest that the SEI film is thinner compared to other regions in the cycled anode. However, the chemical composition of the SEI

films is similar at all locations. After correcting the baseline and normalizing the spectra, the comparison in Supplementary Fig. S6b shows that all the different cycled regions have distinct peaks characteristic of SEI components. These features are commonly found in cycled anodes and can be categorized into three frequency regions: lithium carbonate (Li_2CO_3 1350-1550 cm^{-1}), lithium ethoxide (ROLi 925-1100 cm^{-1}) and lithium hexafluorophospate ($LiPF_6$ 650-900 cm^{-1}).

3.2.2. Raman Spectroscopy

Raman spectra of the baseline anode and the anode harvested from a 1X-Line defect cell are shown in Fig. 4. All the samples showed distinct D, G, and 2D bands, characteristic of graphitic carbon. The uncycled, pristine baseline sample had the lowest fluorescence background. The area of the cycled anode opposite to the 1X-Line defect had significantly less fluorescence compared to the other three cycled anode samples. Fluorescence in Raman spectra of cycled electrodes is common and can originate from multiple sources such as SEI, residual electrolyte, or transition metal complexes.[20]

The Raman spectra of the anodes show contributions from three major components: graphite, carbon black, and fluorescence (Fig. 4). To map the relative contribution of each of these components across the anodes, we assume that the Raman spectra of the composite can be treated as a linear combination of the Raman spectra for these components. Spectra for each pure component were acquired, normalized to the same unit intensity, and used as basis vectors (Fig. 5). This approach to deconvolute the Raman spectra is not quantitative, but provides insights into the relative amount of each component at each location across the map. The maps of the pristine baseline sample are a superposition of the spectra from graphite and carbon black with no fluorescence background at any point on the sample. These maps were similar to the ones obtained opposite to the defect indicating that the sample did not participate in the electrochemical cycling. There were a few islands of high fluorescence on the anode surface opposite the 1X-Line defect. This may be due to residual electrolyte or contamination from the washing process. In the other three cycled electrodes, the Raman maps showed similar uniform distributions of graphite, carbon black, and fluorescence.

3.2.3. X-ray Photoelectron Spectroscopy (XPS)

Fig. 6 shows a comparison of high-resolution XPS spectra and elemental atomic percentages obtained from cycled baseline and 1X-Line defect anodes. All the XPS spectra were obtained after the samples

were subjected to Ar sputtering for 120 s to remove any residual electrolyte and other surface contaminants. Optical images show the sample locations where the XPS spectra were acquired (Supplementary Fig. S7). High-resolution XPS spectra show that the chemical composition of the area opposite to the 1X-Line defect is markedly different from all other cycled anodes (Fig. 6 and Supplementary Fig. S8 and S9). The baseline cycled electrode and other locations on the 1X-Line defect electrode show the typical signatures of SEI formation. The peak at 530.9 in the O1s spectra is assigned to lithium alkoxides and carbonates, while the peak at 528 is from Li_2O (Fig. 6a).[21] Li_2O may not be an intrinsic part of the SEI, since it is formed from Ar^+ ion sputtering of Li_2CO_3.[22] Similarly, the C1s spectra show evidence of carbonates (289.3 eV) and more reduced carbon in the form of graphite and carbon black (284.5 eV) (Fig. 6b). Phosphorus in the form of P-O or P=O is a decomposition product of the PF_6^- anion and is clearly seen in the P 2p spectra at 132.8 eV (Fig. 6e). Significant amounts of manganese are also seen in the Mn 2p and 3p spectra due to crossover from the cathode (Fig. 6c,d). In contrast, the area opposite the 1X-Line defect lacks some of the typical SEI components. Minimal phosphorus and no manganese are observed. The carbon signature is similar to the pristine anode, but significant amounts of lithium (mainly in the form of Li_2O) are still present opposite the defect. This is consistent with the FTIR results that indicate that the SEI that forms opposite to the defect is very thin. In fact, most of the SEI opposite to the defect was probably removed by brief Ar sputtering. This explains why some of the SEI components observed by FTIR are not observed by XPS in the region opposite to the defect. The concentration of Mn near the defect is more than double any of the other cycled anodes (Fig. 6c, d, f), which indicates that cathode particles near the defect are more corroded. Transition metal dissolution is accelerated when the cathode is overcharged and the crystal structure is irreversibly degraded.[23-25]

3.2.4. X-ray Diffraction (XRD) of Cathodes

The crystallinity of the cycled cathodes from the baseline cell were compared with the 1X-Line defect in regions near and far from the line defect (Fig. 7). The diffraction patterns for the baseline cathode and cathode far from the defect showed the expected peaks for $LiNi_{0.5}Mn_{0.3}Co_{0.2}O_2$ (NMC532). They were indexed to the $R\bar{3}m$ space group (α-$NaFeO_2$ -type). The (003) reflection corresponds to the spacing between transition metal layers along the c-axis (Fig. 7b). Far from the defect, the c-lattice parameter is larger for the cathode with the defect compared to the baseline cathode. The cell with the 1X-Line defect showed the most capacity fade after 500 cycles (Fig. 2), and the c-lattice expansion is consistent with

less Li in the lithium layer due to greater loss of lithium inventory. However, near the defect, the c-lattice parameter is smaller compared to the baseline. This is consistent with local overcharging of the NMC cathode, which causes transition metal cations to migrate from octahedral sites in the transition metal layer to octahedral sites in the Li layer. Cation migration causes a phase transformation from a layered structure indexed to the $R\bar{3}m$ space group to a disordered spinel ($LiMn_2O_4$-type) indexed to the $Fd\bar{3}m$ space group.[26] This phase transformation is further confirmed by the appearance of (222) and (440) reflections (Fig. 7c, d). These phase transitions are generally accompanied by oxygen release and transition metal dissolution, consistent with the increased presence of transition metals in the anode opposite to the cathode area near the defect.

To summarize, post-test characterization of the cells with cathode line defects shows that the region of the anode opposite to the defect does not participate in electrochemical cycling, while the cathode becomes locally overcharged near the defect.

(a) FTIR and XPS data show that SEI is formed opposite to the defect, but it is thinner than any other region in the cycled anode.
(b) Raman mapping shows no fluresence opposite to the defect consistent with less electrolyte decomposition and transition metal cross-over.
(c) XPS confirms that Mn crossover is negligible in the region opposite to the defect. However, Mn crossover is accelerated in the region next to the defect. This indicates that the cathode regions adjacent to the defect are more degraded due to local overcharging.
(d) XRD analysis of the cathode near the defect shows evidence for a phase transformation from layered $R\bar{3}m$ to a disordered, spinel-like $Fd\bar{3}m$ structure. This phase transformation is accompanied by transition metal dissolution and crossover, as seen in XPS spectra of the anode.

3.3. Computational Modeling

In order to assess the internal distribution of species in the electrodes and complement the experimental observations, a model of the cell sandwich was built and solved numerically. In order to emphasize local gradients and reduce the size of the problem, a portion of the cell surrounding the line defects was considered and discretized with finite elements (FE). Due to the symmetrical nature of the line defects, the problem was formulated in 2D. Two cases were considered, in addition to the model of planar

electrodes without defects, with schematics shown in Fig. 8. Both geometries were of the same length (15 mm) and had the same material balance.

Fig. 9 compares the results of the calculations depicting the 1X-Line defect and 3X-Line defect with a baseline electrode with no defect. Normalized lithium content is shown at different times during charge as a ratio of current lithium concentration to the maximum concentration in electrode material. When the cell is assembled, all available lithium is contained in the positive electrode, and therefore, the initial state of lithiation of the anode is zero. It can be seen that while the total amount of material remains constant in both cases, more severe misbalance leads to the situation when the negative electrode remains largely unreacted in the area opposite to the uncoated portion of the cathode in the case of 1X-Line defect. This is consistent with results from Raman spectroscopy and XPS, which also show that this region does not participate in electrochemical cycling to the same extent as the rest of the anode. Such a scenario is a consequence of in-plane transport limitations in the electrode, which become more pronounced in the case of wider defect. Futher, on the cathode side we observed excess delithiation of the cathode in the region adjacent to the defect site. The greater degree of delithiation will lead to phase transformations in the cathode structure and accelerate transition metal dissolution and crossover, both of which are experimentally observed. It should be emphasized that the dissolution of Mn from the positive electrode as well as formation of SEI on the negative electrode are not modeled here. The numerical calculations in this work are indended to describe only changes in lithium distribution in the electrodes due to the presence of defects. This information cannot be obtained easily from experiments.

3.4. Proposed Mechanism for Degradation in Cells with Cathode Coating Defects

Combining the experimental observations and results from computational modeling, we can postulate the mechanism for capacity loss and cycle life degradation in cells with line coating defects (Fig. 10). The n/p ratio in the region of the cathode immediately near the defect is locally higher. This leads to overcharging of the cathode near the defect, which causes material degradation over repeated cycling.[27, 28] This degradation is localized at first, but cascades out to other parts of the cathode. The degraded region near the defect participates less in electrochemical cycling, and this effectively leads to an increase in the size of the defective region. This degradation can also be observed by in-depth electrochemical analysis (Supplementary Fig. S10). Area specific impedance calculated from the HPPC protocol (Supplementary Fig. S10a) shows that the cell with the 1X-Line defect exhibits increased

internal resistance after cycling when compared to a baseline cell with no defect. During the last cycle voltage hold (three hours at upper cut-off voltage), the cell with the 1X-Line defect also exhibits larger potential drop (Supplementary Fig. S10b) and much higher residual current (Supplementary Fig. S10c) caused by degradation of the cathode material and anode SEI due to repeated overcharging. From this observation, we can also postulate that the size of the initial defect will influence the rate of degradation, since smaller defective regions do not distort the local n/p ratio as severely. This explains the more rapid fade of the cell with the 1X-Line defect compared to the 3X-Line defect. In the case of different line defects on the anode, substantial lithium plating was observed on the defect site in the anode (Supplementary Fig. S11). The rate of degradation for cells with line defects on the anode was similar regardless of the type of line defect (Supplementary Fig. S12). This indicates the mechanism to be only related to the area of the defect.

4. Conclusion

This study reveals the effect of cathode coating defects on the electrochemical performance of lithium-ion cells. We analyzed four types of defects that commonly occur during the coating process. Electrochemical cycling of cells made with these defects showed that pinholes and agglomerates did not lead to significant loss in capacity. However, cells with non-uniform coatings in the form of line defects showed more severe capacity fade. Post-cycle characterization of the electrodes with one 3 mm line defect showed evidence of significant cathode degradation near the defect region, which is the primary cause for higher capacity loss in these cells. From the results of all the post-cycle analysis, a mechanism was postulated of cascading cathode material degradation originating near the defect as the primary cause for accelerated cell aging. We also propose that the initial size of the defect region affects the rate at which the cathode material degrades over repeated cycling. Electrodes with pinholes, agglomerates, and small line defects may be salvageable, thereby reducing scrap rates and lowering overall manufacturing costs. These electrodes could be used in other applications like grid storage where the demand for power and energy density is not as stringent as in the automotive or electronics industry.

5. Acknowledgement

This research at Oak Ridge National Laboratory, managed by UT Battelle, LLC, for the U.S. Department of Energy (DOE) under contract DE-AC05-00OR22725, was sponsored by the Office of Energy Efficiency and Renewable Energy (EERE) Vehicle Technologies Office (VTO) (Deputy

Director: David Howell) Applied Battery Research subprogram (Program Manager: Peter Faguy). X-ray Diffraction was conducted at the Center for Nanophase Materials Sciences, which is a DOE Office of Science User Facility. Part of this research was supported by the DOE Basic Energy Sciences (BES), Materials Sciences and Engineering Division. The authors would also like to thank Dr. Jianlin Li for helpful technical discussions in designing the experiments that enabled this paper.

6. Author contributions

D.W. and D.M. pursued the idea and D.W. amd L.D. led this research. L.D. performed electrochemical testing and material characterization, analyzed the data, and wrote the manuscript. R.E.R. performed Raman spectroscopy and contributed to analysis and discussion. H.M. collected X-ray photoelectron spectroscopy data, and contributed to analysis and discussion. Y.S. made the NMC electrode, and assisted in electrochemical testing. S.K. performed numerical modeling and contributed to the discussion. C.D. was involved in the technical discussion and editing the manuscript.

7. References

[1] Larcher D, Tarascon JM. Towards greener and more sustainable batteries for electrical energy storage. Nat Chem. 2015;7:19-29.
[2] Martin C. Driving change in the battery industry. Nat Nanotechnol. 2014;9:327-8.
[3] Vora AP, Jin X, Hoshing V, Saha T, Shaver G, Varigonda S, et al. Design-space exploration of series plug-in hybrid electric vehicles for medium-duty truck applications in a total cost-of-ownership framework. Applied Energy. 2017;202:662-72.
[4] Electrochemical Energy Storage Technical Team Roadmap. Department of Energy; 2017.
[5] Howell D. Electrochemical Energy Storage R&D Overview. Department of Energy; 2017.
[6] Li JL, Daniel C, Wood D. Materials processing for lithium-ion batteries. Journal of Power Sources. 2011;196:2452-60.
[7] Li J, Du Z, Ruther RE, An SJ, David LA, Hays K, et al. Toward Low-Cost, High-Energy Density, and High-Power Density Lithium-Ion Batteries. Jom. 2017;69:1484-96.
[8] Jaguemont J, Boulon L, Dubé Y. A comprehensive review of lithium-ion batteries used in hybrid and electric vehicles at cold temperatures. Applied Energy. 2016;164:99-114.
[9] Li L, Dababneh F, Zhao J. Cost-effective supply chain for electric vehicle battery remanufacturing. Applied Energy. 2018;226:277-86.
[10] Wood DL, Li J, Daniel C. Prospects for reducing the processing cost of lithium ion batteries. Journal of Power Sources. 2015;275:234-42.
[11] Du Z, Janke CJ, Li J, Daniel C, Wood DL. Electron Beam Curing of Composite Positive Electrode for Li-Ion Battery. Journal of The Electrochemical Society. 2016;163:A2776-A80.
[12] Cho KY, Kwon YI, Youn JR, Song YS. Evaluation of slurry characteristics for rechargeable lithium-ion batteries. Materials Research Bulletin. 2013;48:2922-6.

[13] Bauer W, Nötzel D. Rheological properties and stability of NMP based cathode slurries for lithium ion batteries. Ceramics International. 2014;40:4591-8.
[14] Harris SJ, Lu P. Effects of Inhomogeneities—Nanoscale to Mesoscale—on the Durability of Li-Ion Batteries. The Journal of Physical Chemistry C. 2013;117:6481-92.
[15] Müller S, Eller J, Ebner M, Burns C, Dahn J, Wood V. Quantifying Inhomogeneity of Lithium Ion Battery Electrodes and Its Influence on Electrochemical Performance. Journal of The Electrochemical Society. 2018;165:A339-A44.
[16] Mohanty D, Hockaday E, Li J, Hensley DK, Daniel C, Wood DL. Effect of electrode manufacturing defects on electrochemical performance of lithium-ion batteries: Cognizance of the battery failure sources. Journal of Power Sources. 2016;312:70-9.
[17] Doyle M, Fuller TF, Newman J. Modeling of Galvanostatic Charge and Discharge of the Lithium/Polymer/Insertion Cell. Journal of The Electrochemical Society. 1993;140:1526-33.
[18] Lu Z, Beaulieu LY, Donaberger RA, Thomas CL, Dahn JR. Synthesis, Structure, and Electrochemical Behavior of Li[Ni[sub x]Li[sub 1/3−2x/3]Mn[sub 2/3−x/3]]O[sub 2]. Journal of The Electrochemical Society. 2002;149:A778.
[19] Harris SJ, Timmons A, Baker DR, Monroe C. Direct in situ measurements of Li transport in Li-ion battery negative electrodes. Chemical Physics Letters. 2010;485:265-74.
[20] Jeon K-J, Lee Z, Pollak E, Moreschini L, Bostwick A, Park C-M, et al. Fluorographene: A Wide Bandgap Semiconductor with Ultraviolet Luminescence. ACS Nano. 2011;5:1042-6.
[21] Ciosek Högström K, Malmgren S, Hahlin M, Gorgoi M, Nyholm L, Rensmo H, et al. The Buried Carbon/Solid Electrolyte Interphase in Li-ion Batteries Studied by Hard X-ray Photoelectron Spectroscopy. Electrochimica Acta. 2014;138:430-6.
[22] Edström K, Herstedt M, Abraham DP. A new look at the solid electrolyte interphase on graphite anodes in Li-ion batteries. Journal of Power Sources. 2006;153:380-4.
[23] Pieczonka NPW, Liu Z, Lu P, Olson KL, Moote J, Powell BR, et al. Understanding Transition-Metal Dissolution Behavior in LiNi0.5Mn1.5O4 High-Voltage Spinel for Lithium Ion Batteries. The Journal of Physical Chemistry C. 2013;117:15947-57.
[24] Wandt J, Freiberg A, Thomas R, Gorlin Y, Siebel A, Jung R, et al. Transition metal dissolution and deposition in Li-ion batteries investigated by operando X-ray absorption spectroscopy. Journal of Materials Chemistry A. 2016;4:18300-5.
[25] Zheng H, Sun Q, Liu G, Song X, Battaglia VS. Correlation between dissolution behavior and electrochemical cycling performance for LiNi1/3Co1/3Mn1/3O2-based cells. Journal of Power Sources. 2012;207:134-40.
[26] Bak SM, Hu E, Zhou Y, Yu X, Senanayake SD, Cho SJ, et al. Structural changes and thermal stability of charged LiNixMnyCozO(2) cathode materials studied by combined in situ time-resolved XRD and mass spectroscopy. ACS Appl Mater Interfaces. 2014;6:22594-601.
[27] Takamura T, Saito M, Shimokawa A, Nakahara C, Sekine K, Maeno S, et al. Charge/discharge efficiency improvement by the incorporation of conductive carbons in the carbon anode of Li-ion batteries. Journal of Power Sources. 2000;90:45-51.
[28] Cannarella J, Arnold CB. The Effects of Defects on Localized Plating in Lithium-Ion Batteries. Journal of The Electrochemical Society. 2015;162:A1365-A73.

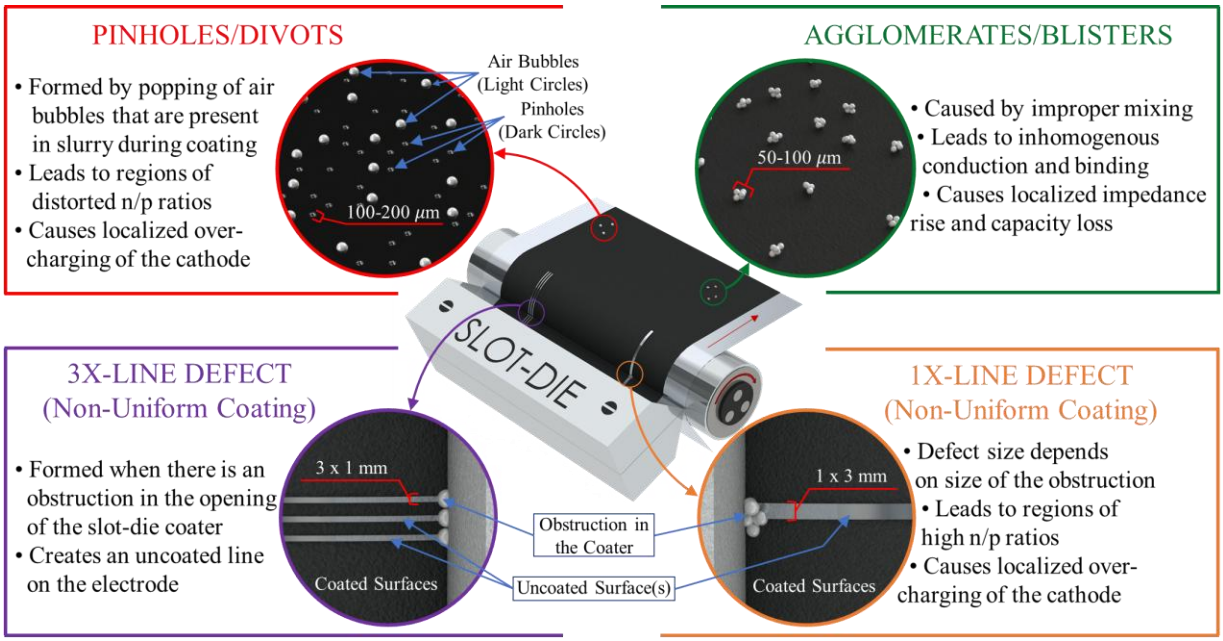

Figure 1. Schematic showing the formation of defects like pinholes or divots, agglomerates or blisters and line defects or non-uniform coating during the electrode coating process. The schematic explains the impact of cathode defects, but analogous issues are expected for anode defects. In this study, pinholes were formed by manually removing material from coated electrodes and agglomerates were formed by modifying the slurry mixing procedure. Line defects were coated using a special type of shim in the slot-die coating machine to mimic obstructions in the coater. Two sizes of line defects were analyzed: one large uncoated line and three smaller uncoated lines. Both line defects removed equal amounts of material.

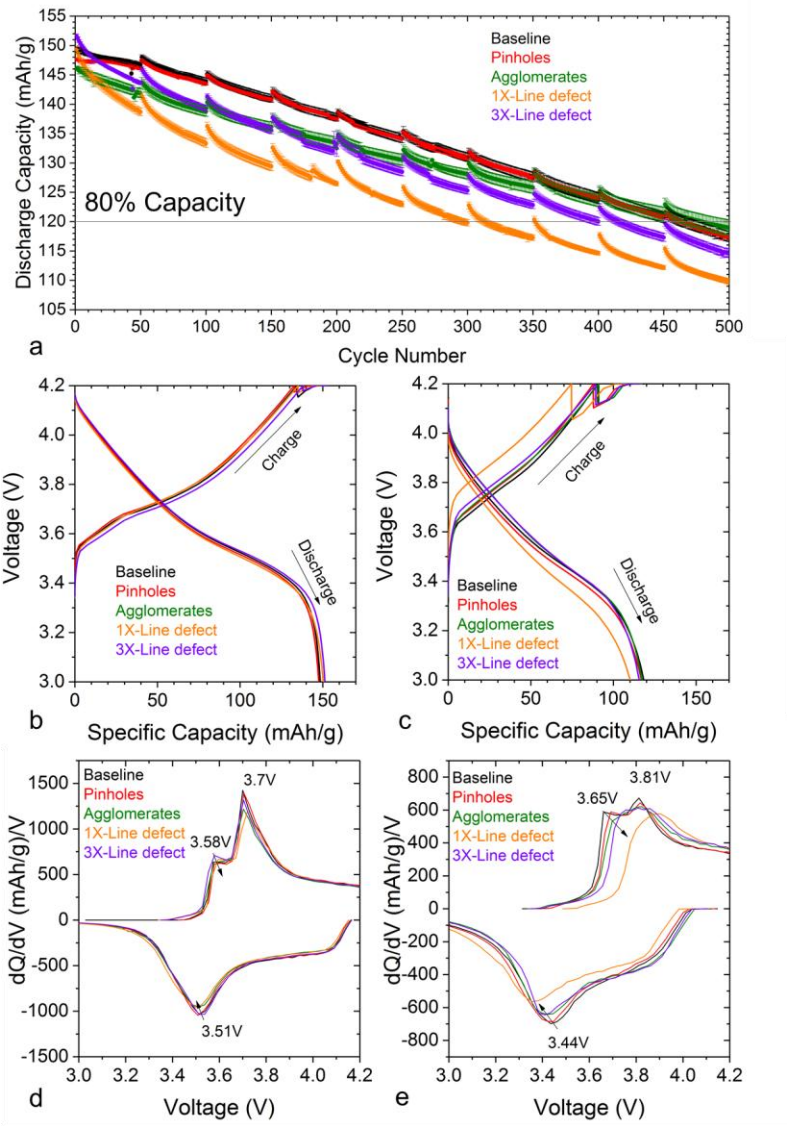

Figure 2. Electrochemical cycling data for cells with electrode coating defects. (a) Cycle life plot comparing the discharge capacities of baseline cells (Black) with four different types of defects: Pinholes (Red), Agglomerates (Green), 1X-line defect (Orange) and 3X-line defect (Purple). Cycling was performed between 3-4.2 V with a 3 h voltage hold at the top of each charging step in order to accelerate cell degradation. The break in cycling at every 50 cycles is due to HPPC analysis. Three cells were tested for each type of electrode coating defect and error bars in each cycle is indicated. Charge/discharge curves of various defects and baseline at the (b) 1st cycle and (c) 500th cycle in the long-term cycling test. Differentiated capacity curves of various defects and baseline at the (d) 1st cycle and (e) 500th cycle. The charge discharge curves and dQ/dV profiles were plotted from one representative cell for each kind of defect.

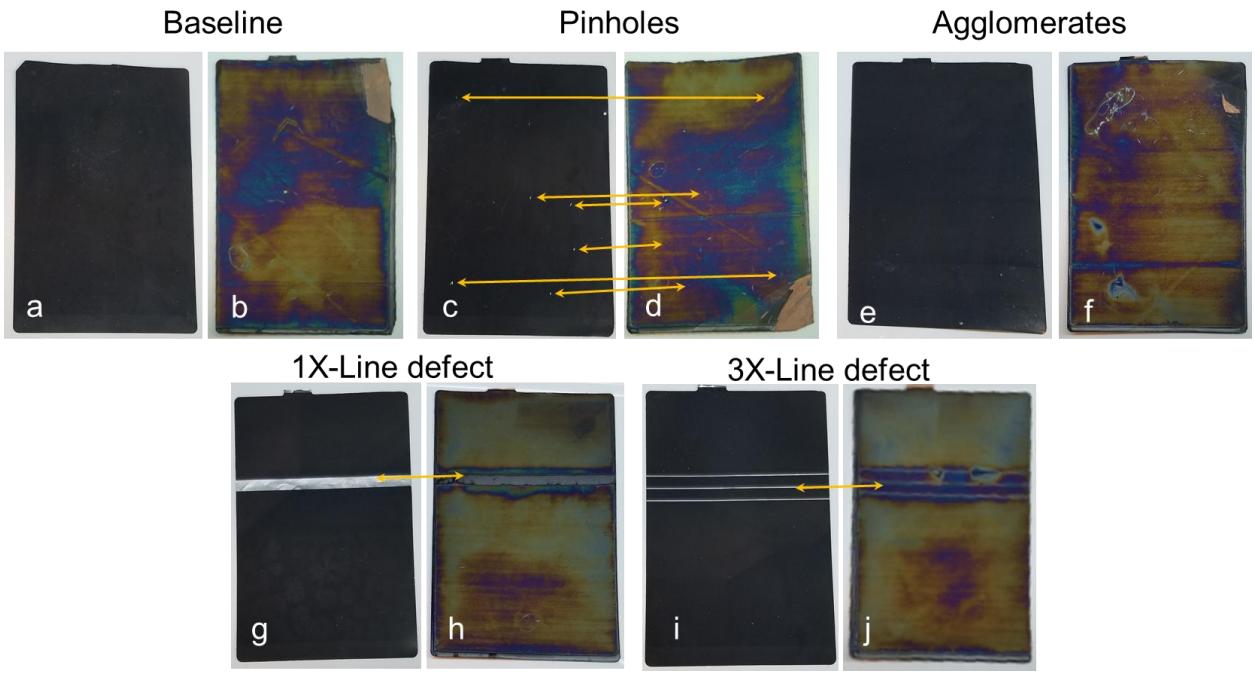

Figure 3. Optical images of disassembled cathodes with corresponding anodes of (a,b) baseline, (c,d) pinholes, (e,f) agglomerates, (g,h) 1X-line defect, (i,j) 3X-line defect after 500 cycles at 1C/1C rate using a harsh cycling protocol. A small amount of anode delaminated at the corners during cell disassembly. The electrodes were rinsed in DEC solvent for 1 mins to remove residual salt and other contaminants. Trapped Li in the anode causes changes in color to red/blue (partial lithiation) and gold (complete lithiation).

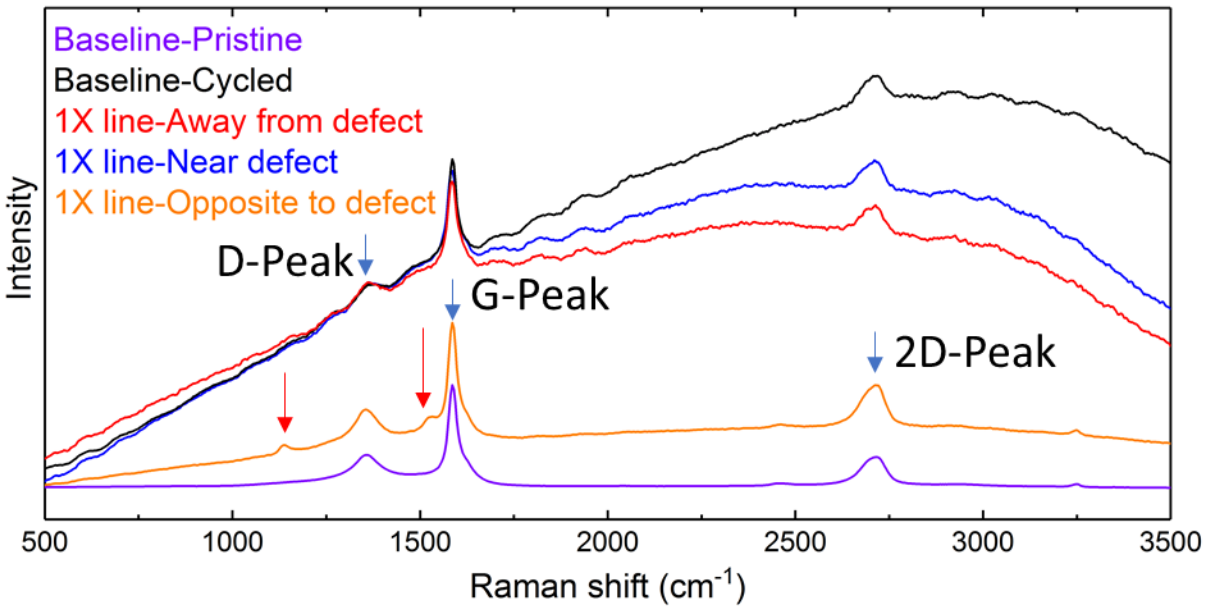

Figure 4. Raman spectra comparing cycled anodes with defects to baseline cycled and uncycled anodes. The D-peak, G-peak and 2D-peak of graphitic carbon are indicated. The large fluorescence background in the cycled anode is from the SEI compounds formed during cycling. The two peaks marked in red are from components in the binder unrelated to this study.

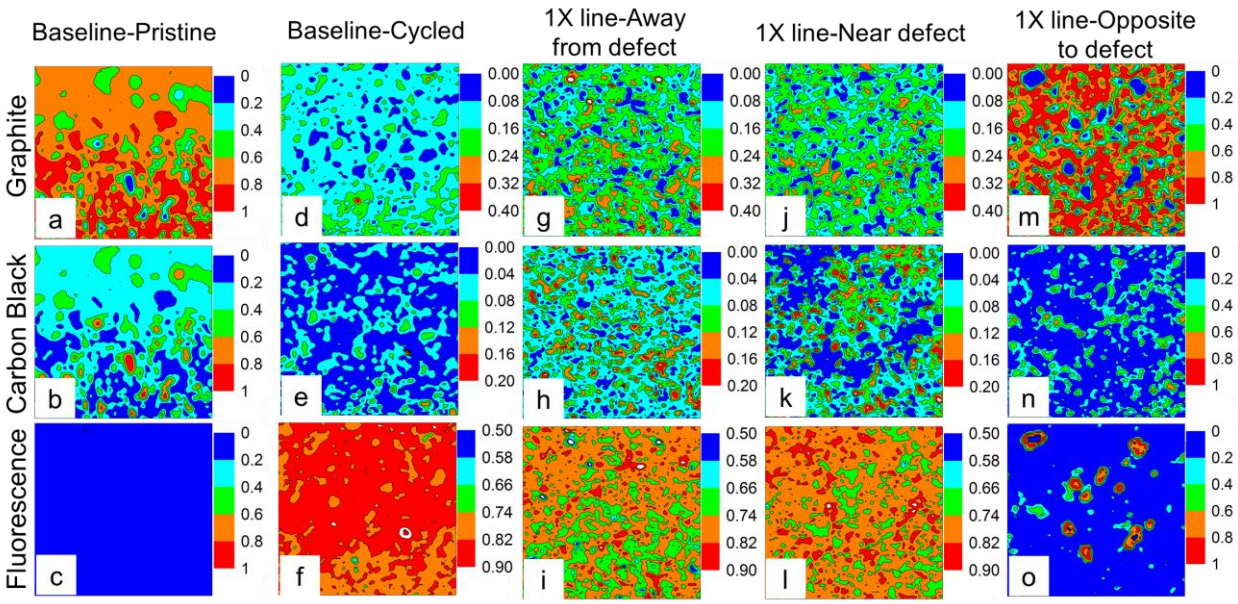

Figure 5. Raman maps comparing the pristine baseline with all cycled anodes, which were generated by fitting the Raman spectrum from each point to three different components: (1) Graphite, (2) Carbon black and (3) Fluorescence background. The scale bars indicate the spectral fraction of each component at each point in the sample.

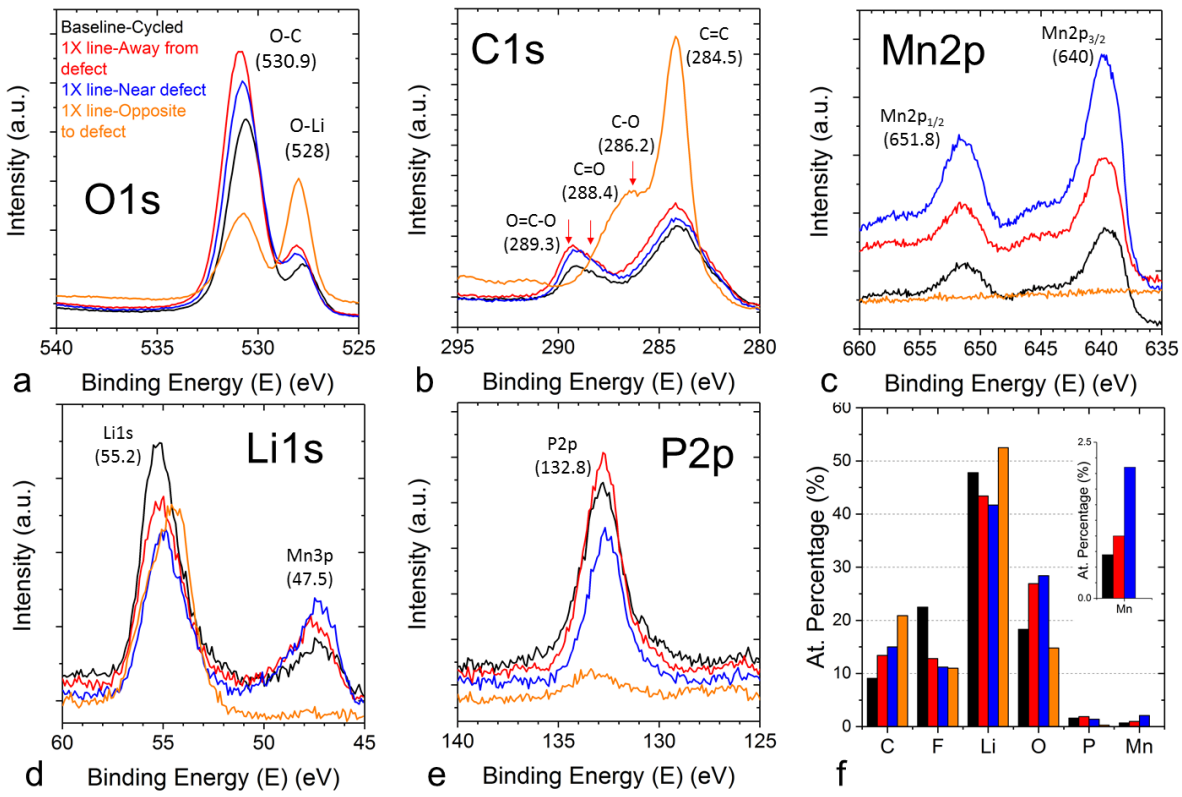

Figure 6. Data comparing (a) O 1s, (b) C 1s, (c) Mn 2p, (d) Li 1s and (e) P 2p high-resolution XPS spectra of all cycled anodes from cells with defects and the cycled baseline cell. (f) Atomic percentage of each element detected using XPS. The insert shows the magnified comparison plot of Mn atomic percentage in different cycled anodes. All XPS data were obtained after Ar^+ ion sputtering for 120 s to remove residual electrolyte and other surface contamination.

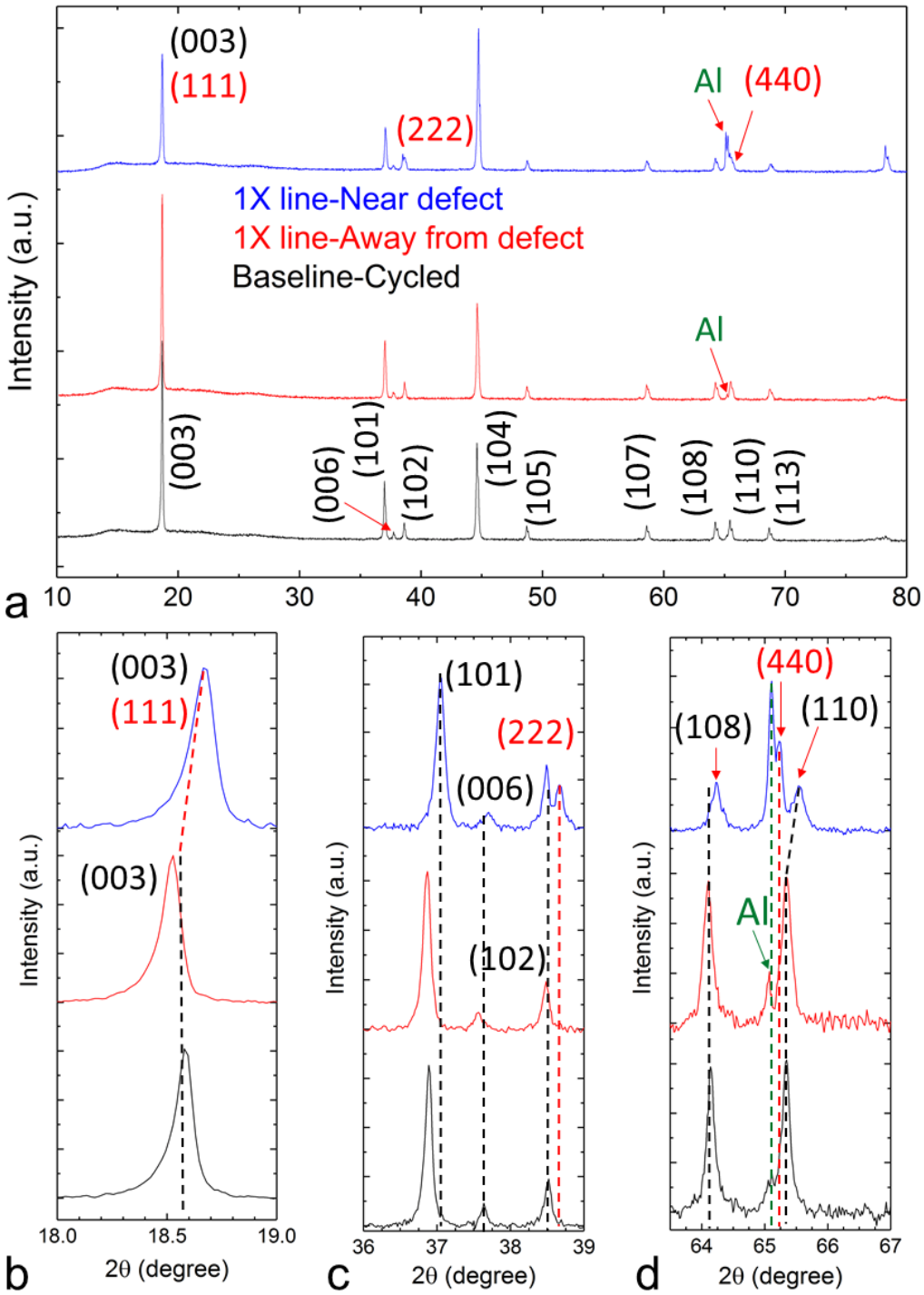

Figure 7. (a) Comparison of XRD patterns from cycled cathodes. (b, c, d) Magnified regions showing the peaks indexed by the $R\bar{3}m$ space group in all the cycled electrodes along with appearance of (b) (111), (c) (222) and (d) (440) peaks indexed by the $Fd\bar{3}m$ space group in the region of electrode near the defect. Aluminum from the current collector is marked in the plot.

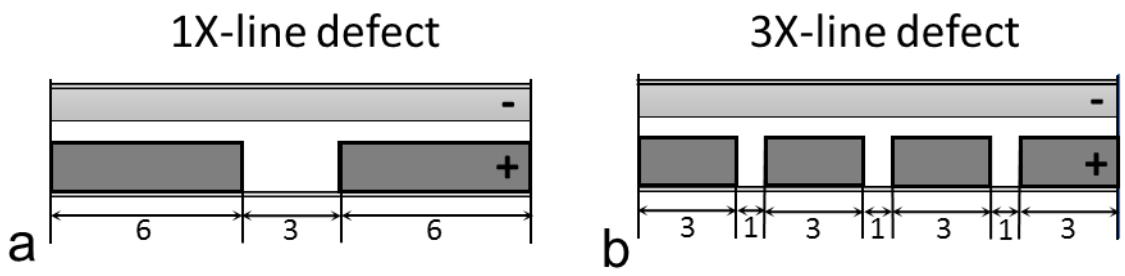

Figure 8. Schematics (not to scale) of the simulated configurations (a) 1X-line defect, and (b) 3X-line defect. Dimensions are in mm.

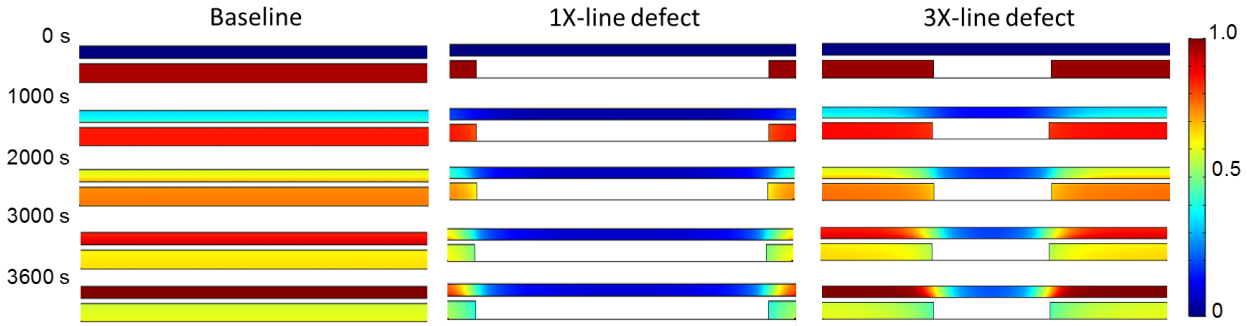

Figure 9. Comparision showing local lithium concentration in electrode materials at different times during the first charge cycle for cells with and without line defects. Scale shows normalized lithium content.

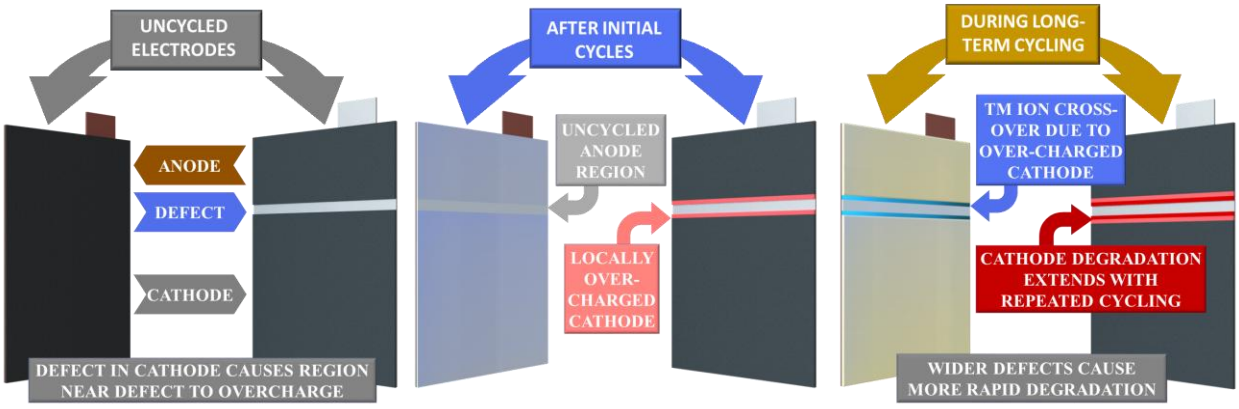

Figure 10. Schematic showing the mechanism of electrode degradation in both cathode and anode due to the presence of the line defect on the cathode.

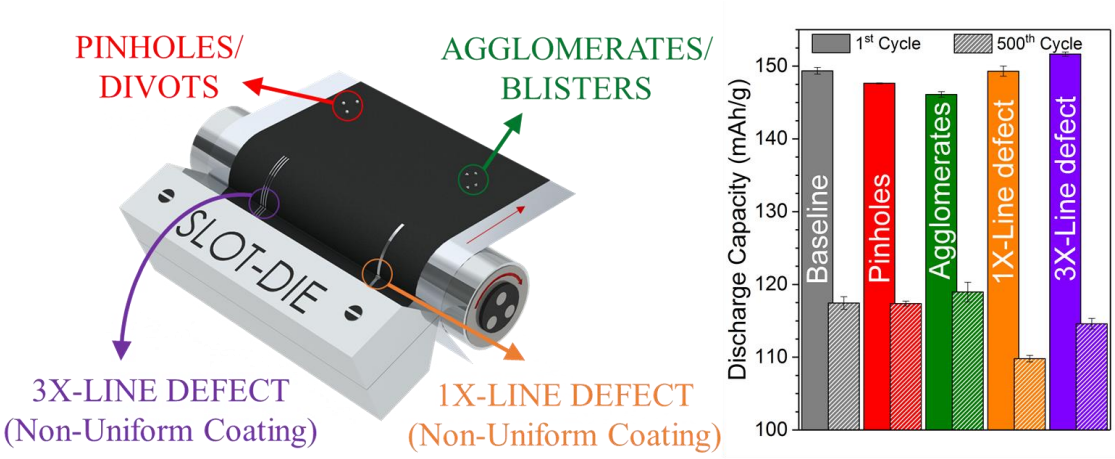

TOC